

# Optimization of magnetoresistive sensor current for on-chip magnetic bead detection using the sensor self-field



Anders Dahl Henriksen, Giovanni Rizzi, Frederik Westergaard Østerberg, Mikkel Fougt Hansen\*

Department of Micro- and Nanotechnology, Technical University of Denmark, DTU Nanotech, Building 345 East, DK-2800 Kongens Lyngby, Denmark

## ARTICLE INFO

### Article history:

Received 25 June 2014

Received in revised form

24 September 2014

Accepted 29 September 2014

Available online 1 October 2014

### Keywords:

Joule heating

Magnetoresistive sensor

Magnetic biosensor

Thermal modeling

Planar Hall effect

## ABSTRACT

We investigate the self-heating of magnetoresistive sensors used for measurements on magnetic beads in magnetic biosensors. The signal from magnetic beads magnetized by the field due to the sensor bias current is proportional to the bias current squared. Therefore, we aim to maximize the bias current while limiting the sensor self-heating. We systematically characterize and model the Joule heating of magnetoresistive sensors with different sensor geometries and stack compositions. The sensor heating is determined using the increase of the sensor resistance as function of the bias current. The measured temperature increase is in good agreement with a finite element model and a simple analytical thermal model. The heat conductance of our system is limited by the 1  $\mu\text{m}$  thick electrically insulating silicon dioxide layer between the sensor stack and the underlying silicon wafer, thus the heat conductance is proportional to the sensor area and inversely proportional to the oxide thickness. This simple heat conductance determines the relationship between bias current and sensor temperature, and we show that 25  $\mu\text{m}$  wide sensor on a 1  $\mu\text{m}$  oxide can sustain a bias current of 30 mA for an allowed temperature increase of 5  $^{\circ}\text{C}$ . The method and models used are generally applicable for thin film sensor systems. Further, the consequences for biosensor applications of the present sensor designs and the impact on future sensor designs are discussed.

© 2014 Elsevier B.V. All rights reserved.

## 1. Introduction

In recent years magnetic beads have become a viable alternative to fluorescent labels for both diagnostics and research purposes [1]. Magnetic beads are most often used in a sandwich assay, replacing fluorescent tags, such that the presence of the biological analyte can be detected indirectly via the magnetic field from the magnetic beads attached to the sensor surface. This magnetic field can be detected by magnetoresistive (MR) sensors [2–5]. We have previously demonstrated the use of planar Hall effect bridge (PHEB) sensors in a magnetic bead-based readout for on-chip DNA detection using both volume- and surface-based detection schemes [6–8]. In these studies, the magnetic beads were magnetized by the field arising from the sensor bias current. This eliminates the need for external electromagnets and ensures that the signal from a magnetic bead is positive for all bead positions with respect to the sensor [9].

For both surface- and volume-based detection the signal is proportional to the current squared. Therefore, a higher current

means a higher signal and thereby a higher sensitivity assuming that the signal-to-noise ratio is limited by the noise of the readout electronics. However, high currents can cause a breakdown of the sensors due to failure of the sensor coating and will lead to increased Joule heating. Thus, it is of general interest to know the maximum current that can be used without affecting the experiment.

In this paper, we present a systematic study of the self-heating of PHEB magnetoresistive sensors in order to maximize the signal from magnetic beads. We first characterize the temperature dependence of the sensor bridge resistance. This knowledge is used to determine the sensor temperature increase due to Joule heating as function of the sensor bias current. The relation between sensor temperature and bias current is compared to two simplified analytical models as well as a finite element model of the heat transport through the underlying silicon wafer. The simple models are found to be in good agreement with the data and consequences for applications and future designs are discussed. As the models are generally applicable, they can be used to give an estimate of the expected heating from any current and any sensor geometry. These results are relevant for the application of magnetoresistive sensors for characterization of magnetic beads as well as for biodetection applications.

\* Corresponding author.

E-mail address: [Mikkel.Hansen@nanotech.dtu.dk](mailto:Mikkel.Hansen@nanotech.dtu.dk) (M.F. Hansen).

## 2. Theory

### 2.1. Planar Hall effect bridge sensors

The sensors are based on the anisotropic magnetoresistance of permalloy ( $\text{Ni}_{80}\text{Fe}_{20}$ ) and are designed in a Wheatstone bridge geometry with four sensor stripes, each having a width  $w$  and length  $l$  as illustrated in Fig. 1. The sensor stack, also given in Fig. 1, is exchange-pinned along the  $x$ -direction using  $\text{Mn}_{80}\text{Ir}_{20}$  to define a unique magnetization orientation in zero applied magnetic field. The sensor bridge is biased using a current  $I_x$  applied along the  $x$ -direction. The bridge resistance  $R$  is obtained from the voltage drop  $V_x$  measured along the  $x$ -direction as  $R = V_x/I_x$ . When used for sensing of magnetic fields, the planar Hall effect signal  $V_y$  can be written as [10]

$$V_y = S_0 I_x H_y, \quad (1)$$

where  $S_0$  is the low-field sensitivity and  $H_y$  is the average magnetic field experienced by the sensor in the  $y$ -direction. In the presence of magnetic beads that show a linear magnetic field response and in zero externally applied magnetic field, this field can be written as  $H_y = \gamma I_x$ , where  $\gamma$  depends on the sensor stack and geometry, the amount and distribution of magnetic beads near the sensor surface and the magnetic bead properties [6,9]. Thus, the sensor signal due to magnetic beads can be written as

$$V_y = S_0 \gamma I_x^2, \quad (2)$$

where it is noted that this signal is proportional to  $I_x^2$ .

### 2.2. Sensor self-heating

For a moderate temperature change, the bridge resistance depends linearly on the temperature  $T$ :

$$R(T) = R_0(1 + \alpha(T - T_0)) \quad (3)$$

where  $R_0$  is the resistance at  $T = T_0$  and  $\alpha$  is the temperature coefficient.

The Joule heating in the PHEB sensor due to the applied sensor current is

$$P_{\text{heating}} = R(I_x) I_x^2 \quad (4)$$

where we have explicitly written the bias current dependence of the bridge resistance.

The heat transportation through a material due to a temperature difference  $\Delta T = T - T_0$  with respect to the surroundings is

$$P_{\text{dissipation}} = G_{\text{eff}} \Delta T \quad (5)$$

where  $G_{\text{eff}}$  is the effective thermal conductance. In equilibrium, the dissipated power must equal the Joule heating and thus the resistance and temperature difference are given by

$$R(I_x) = \frac{R_0}{1 - \alpha R_0 I_x^2 / G_{\text{eff}}} \quad (6)$$

$$\Delta T = \frac{1}{\frac{G_{\text{eff}}}{R_0 I_x^2} - \alpha} \quad (7)$$

For the sensor stack in Fig. 1, we expect that heat dissipation through the silicon dioxide beneath the sensor stack will be the dominating pathway for heat dissipation as the oxide is thin and silicon is a good thermal conductor. Because the thickness of the  $\text{SiO}_2$  layer is much smaller than the sensor width, we expect the heat-flow to be approximately vertical through the  $\text{SiO}_2$  under the sensor. In this case the heat conductance is given by

$$G_{\text{SiO}_2} = \kappa_{\text{SiO}_2} (4wl) / t_{\text{SiO}_2}, \quad (8)$$

where  $\kappa_{\text{SiO}_2}$  is the thermal conductivity (bulk value  $\kappa_{\text{SiO}_2} = 1.4 \text{ W}/(\text{m}^\circ\text{C})$ ) and  $t_{\text{SiO}_2}$  is the thickness of the silicon dioxide.

We further expand the model to also include the silicon wafer in the heat network. The width of the resistor elements is small compared to the wafer thickness, and we can therefore approximate them in a thermal calculation on the wafer cross-section as a point source. Moreover, we assume heat to flow radially away from the sensor resistor into the wafer. This radial heat flow can be approximated as heat conductance through a cylinder shell running along the resistor with inner radius  $r_{\text{inner}} = w/2$  and outer radius  $r_{\text{outer}} = t_{\text{wafer}}$ , see Fig. 3 for an illustration. Including this approximation, the combined heat conductance is

$$G_{\text{Si+SiO}_2}^{-1} = \frac{t_{\text{SiO}_2}}{\kappa_{\text{SiO}_2} (4wl)} + \frac{\ln(2t_{\text{wafer}}/w)}{\kappa_{\text{Si}} \pi 4l}, \quad (9)$$

where  $\kappa_{\text{Si}}$  is the thermal conductivity of silicon (bulk value  $\kappa_{\text{Si}} = 149 \text{ W}/(\text{m}^\circ\text{C})$ ).

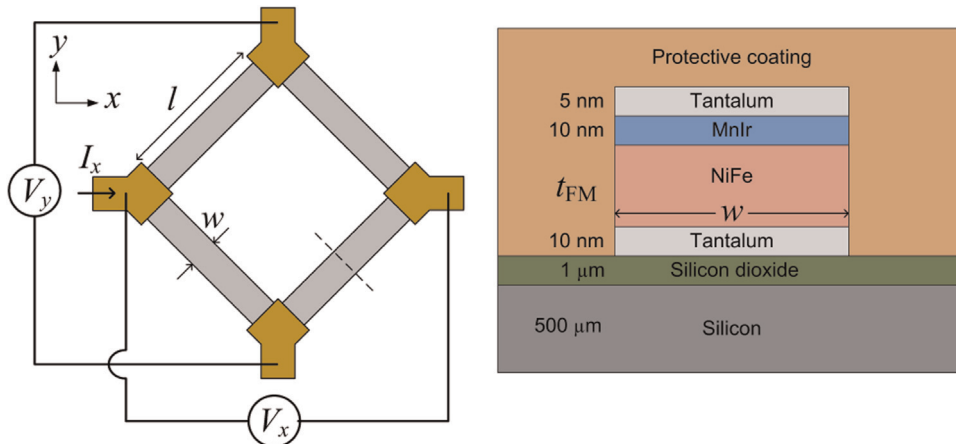


**Fig. 1.** Illustration of the sensor geometry and the sensor stack with definitions of geometrical and electrical parameters. The right panel shows a cross-section of a sensor arm (shown by the dashed line in the left panel). In the present study, we have used  $t_{\text{FM}} = 10, 20$  or  $30 \text{ nm}$ .

### 3. Methods

#### 3.1. Experimental Setup

Three wafers were fabricated of the stack seen in Fig. 1 with permalloy thicknesses of  $t_{\text{FM}} = 10, 20$  and  $30$  nm. The magnetic stacks were deposited in a Kurt J. Lesker CMS-18 magnetron sputter system on a silicon wafer of thickness  $t_{\text{wafer}} = 500 \mu\text{m}$  with a thermal oxide of thickness  $t_{\text{SiO}_2} = 1 \mu\text{m}$ , and defined by lift-off as described previously [6,10]. A contact layer of Ti (10 nm)/Pt (100 nm)/Au (100 nm)/Ti (10 nm) was deposited by e-beam evaporation and defined by lift-off. To ensure sensor operation in liquids, the sensor was protected by a coating of Ormocomp (Micro Resist Technology GmbH, Germany) with a thickness  $t_{\text{coating}} = 1 \mu\text{m}$  defined by spin-coating and patterned by UV lithography. A chip with five different PHEB sensors was used for each measurement. The sensors had a fixed length of  $l = 250 \mu\text{m}$  and different widths of  $w = 5, 10, 15, 20$  and  $25 \mu\text{m}$ . The chip was integrated in a lab-on-a-chip system and placed in an aluminum well with heat sink grease (Circuit Works® CT40-5), see Fig. 2. This well is connected via a Cu stub to a Peltier element, controlled by a Wavelength Electronics LFI-3751 temperature controller. The Pt1000 thermoresistive control thermometer is placed just below the aluminum

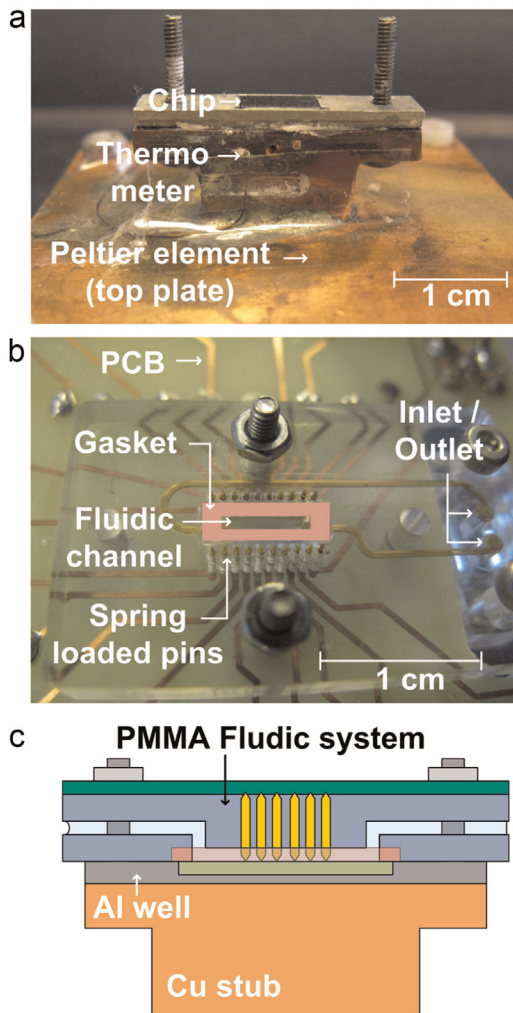


**Fig. 2.** (a) Picture of a chip in the temperature controlled aluminum well on top of the Cu stub and Peltier element. (b) Picture of the PMMA top and printed circuit board for electrical connections (seen through the top). The part observed faces the sensor chip and provides electrical contact via spring-loaded pins and defines the fluid channel over the sensor chip using a PDMS gasket. (c) Schematic cross-section of the assembled fluidic system (not to scale).

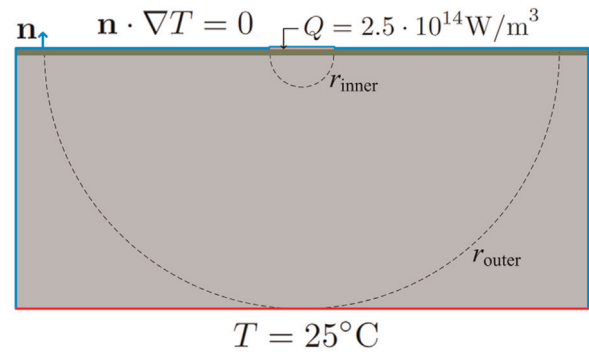


**Fig. 3.** 2D COMSOL model of a cross-section of a sensor arm. The sensor arm cross-section, shown approximately to scale at the top, is modeled as a uniform heat source. Heat conduction through the chip mount is neglected. (For interpretation of the references to color in this figure caption, the reader is referred to the web version of this article.)

well. This assured excellent thermal contact between the sensor, Cu stub and thermometer, and the chip resistance reaches its steady-state in less than a second after the control thermometer. Further, the thermal conductance of the Cu stub is high enough to make any temperature gradient over the stub negligible. Moreover, the large thermal mass of the Cu stub ensures that a local on-chip heating of a sensor has a negligible influence on the temperature of the Cu stub. Electrical contact to the chip was made through spring-loaded pins placed in a machined polymer top that also defined the fluidic channel over the sensors [11]. The sensor current was provided by a Keithley 2400 SourceMeter that also measured the sensor bridge resistance.

#### 3.2. Finite element thermal modeling

A 2D COMSOL simulation was made to facilitate comparison of the full geometry and corresponding heat currents to the simple heat networks of Eqs. (8) and (9). The model (Fig. 3) consists of a nickel domain (pink domain in Fig. 3;  $w \times 55$  nm) on a silicon-dioxide domain (green domain;  $2000 \mu\text{m} \times 1 \mu\text{m}$ ) on top of a silicon domain (gray domain;  $2000 \mu\text{m} \times 500 \mu\text{m}$ ). This emulates a sensor with  $t_{\text{FM}} = 30$  nm and corresponds to the cross-section shown by a dashed line in the left panel of Fig. 1. The bottom boundary of the silicon domain was set to  $25 \text{ }^\circ\text{C}$  (red boundary in Fig. 3) while all other boundaries were set to insulating (blue boundary),  $\mathbf{n} \cdot \nabla T = 0$ , with  $\mathbf{n}$  being the normal vector. As there is air directly above the sensor surface and the polymer mount for the electrical contacts is well separated from the sensor arm, the assumption of thermal insulation is well justified. The nickel domain was changed to a uniform heat source,  $Q$ . All material parameters were taken from the COMSOL material library. The width of the nickel domain was varied from  $5 \mu\text{m}$  to  $25 \mu\text{m}$  and the steady-state mean nickel temperature was recorded for each configuration, which was used to calculate the heat conductance of the system.

## 4. Results

#### 4.1. Bridge resistance vs. temperature

We used the sensor resistance  $R(T) = V_x/I_x$  as a thermometer for the chip. However, to do this we first measured the temperature coefficient,  $\alpha$ , for each chip. Using the external temperature control, the sensor bridge resistance was measured at five different temperatures between  $20$  and  $50 \text{ }^\circ\text{C}$ . The dependence of the bridge resistance on temperature can be seen in Fig. 4 for  $t_{\text{FM}} = 30$  nm. The resistance showed a linear temperature

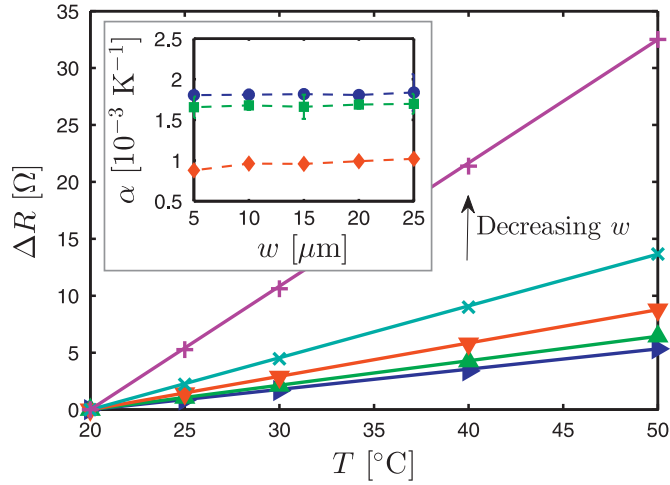


**Fig. 4.** Measured change in sensor bridge resistance vs. temperature for the wafer with  $t_{\text{FM}}=30$  nm and  $w=5, 10, 15, 20$  and  $25$   $\mu\text{m}$ . Fits of Eq. (3) to the data are shown as solid lines. The inset shows the temperature coefficients,  $\alpha$ , extracted from fits for all wafers and sensor widths; blue circles, green squares and red diamonds correspond to  $t_{\text{FM}}=30, 20$  and  $10$  nm, respectively. (For interpretation of the references to color in this figure caption, the reader is referred to the web version of this article.)

dependence according to Eq. (3) for all chips and the fitted temperature coefficients for all investigated sensors can be seen in the inset of Fig. 4. For the sensors from a given wafer, the variation of the measured temperature coefficients is small and no dependence on the sensor width is observed. This confirms that the bridge resistance is dominated by the sensor resistance (i.e., that the series resistance of the contacts and the connectors is negligible). The temperature coefficient, however, does depend on the stack composition and a higher temperature coefficient is observed for higher permalloy thickness.

#### 4.2. Bridge self-heating vs. bias current

Next, we measured the bridge resistance while increasing the bias current  $I_x$ . The bias current gives rise to Joule heating and thus increased resistance for high bias currents. The relationship between the resistance and current was fitted to Eq. (6) with  $R_0$  and  $G_{\text{eff}}$  as free fitting parameters. The resistance increase was converted to a temperature increase using the temperature coefficients determined in Fig. 4. Fig. 5 shows the temperature increase, obtained for the wafer with  $t_{\text{FM}}=30$  nm, vs.  $I_x$  for the indicated values of  $w$ . The black lines are plots of Eq. (7) with the values of  $R_0$  and  $G_{\text{eff}}$  obtained from fits of Eq. (6) to  $R(I_x)$  vs.  $I_x$  data. Excellent agreement between the linear theory and data is observed for all stacks and sensors.

From Fig. 5 one can also find a maximum sensor current if a known limit for the acceptable sensor self-heating is defined, for example by the bioassay requirements. The horizontal dashed line in Fig. 5 indicates a maximum allowed temperature increase chosen arbitrarily to  $5^\circ\text{C}$ . Fig. 6 shows the maximum allowed currents  $I_{\Delta T}$  giving rise to sensor temperature increases of  $\Delta T=1^\circ\text{C}$  and  $\Delta T=5^\circ\text{C}$ , as function of the sensor width  $w$  for the indicated permalloy thicknesses. The values of  $I_{\Delta T}$  are observed to increase approximately linearly with the sensor width with a slope that increases with the permalloy thickness. For example, for  $t_{\text{FM}}=30$  nm and  $w=25$   $\mu\text{m}$ , which are the values used in our recent studies [6,8], we find that  $I_{\Delta T=1^\circ\text{C}} \approx 16$  mA and  $I_{\Delta T=5^\circ\text{C}} \approx 36$  mA.

The maximum applicable power is limited by the effective heat conduction of the setup,  $P_{\text{max}}(\Delta T) = G_{\text{eff}}\Delta T$ . We obtained values of

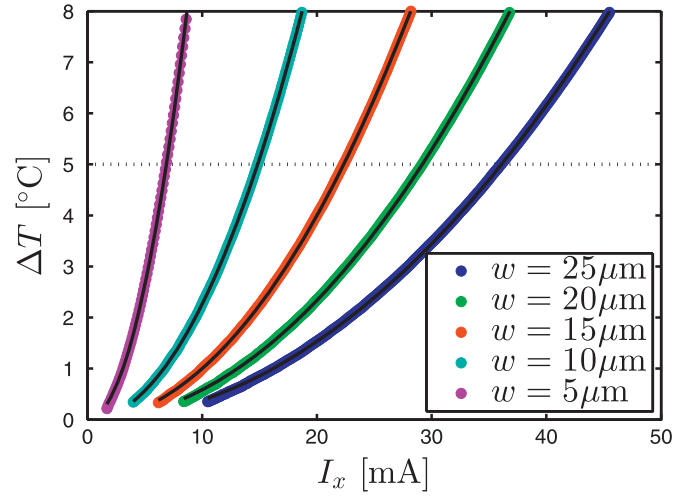


**Fig. 5.** The sensor temperature increase vs. the sensor current for the wafer with  $t_{\text{FM}}=30$  nm. The black lines are plots of Eq. (7) with the values of  $R_0$  and  $G_{\text{eff}}$  obtained from fits of Eq. (6) to  $R(I_x)$  vs.  $I_x$  data. The PID controller was set to  $T=25^\circ\text{C}$ . The horizontal line indicates a maximum allowed temperature increase of  $5^\circ\text{C}$ .

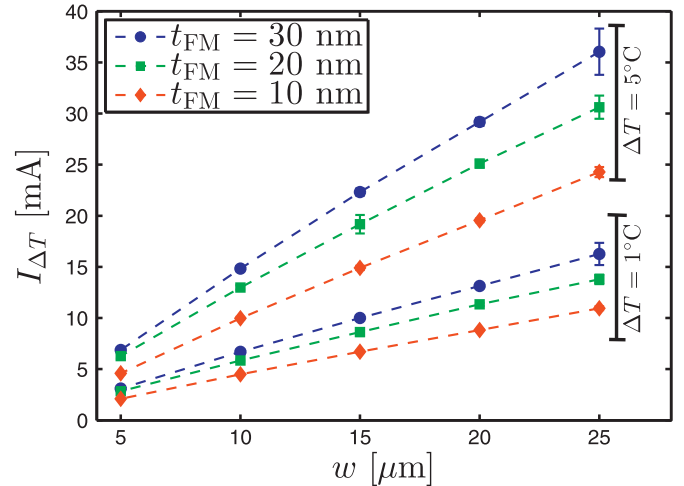


**Fig. 6.** Values of the maximum allowed current  $I_{\Delta T}$  that keeps the sensor self-heating below  $\Delta T=1^\circ\text{C}$  and  $\Delta T=5^\circ\text{C}$  as function of the sensor width  $w$  for the indicated permalloy thicknesses. All sensors had a length of  $l=250$   $\mu\text{m}$ . The dashed lines are guides to the eye.

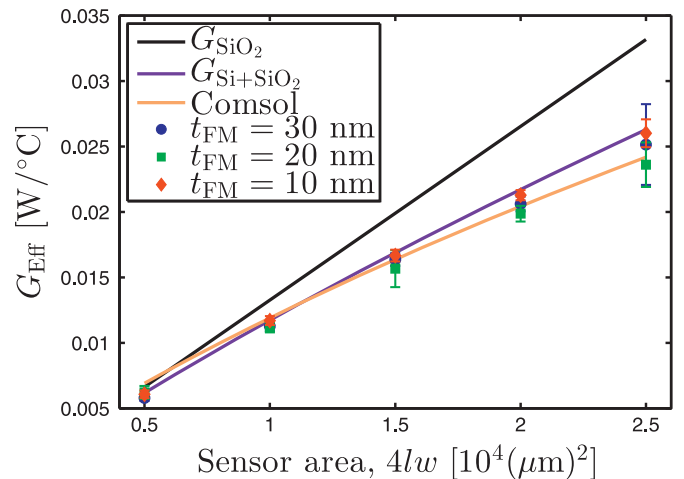


**Fig. 7.** The effective heat conduction  $G_{\text{eff}}$  obtained for all sensors as well as the theoretical predictions of Eqs. (8) and (9) and the COMSOL model for  $t_{\text{FM}}=30$  nm.

$G_{\text{eff}}$  from fits of Eq. (6) to all measurements of  $R(I_k)$  vs.  $I_x$ . Fig. 7 shows the obtained values as function of the sensor area  $4lw$  for all sensor stacks as well as the predictions of the two simple analytical models (Eqs. (8) and (9)) and the COMSOL model (cf. Section 3.2). The value of  $G_{\text{eff}}$  is found to be only little sensitive to the value of  $t_{\text{FM}}$ . This is in agreement with expectations as the lateral heat transport through the magnetic stack is small compared to the vertical heat flow due to the comparably small cross-section of the stack.

## 5. Discussion

### 5.1. Thermal modeling

In this section, we discuss the validity of the thermal modeling and the limitations of the simple thermal models, Eqs. (8) and (9), where the heat resistance is dominated by the silicon dioxide or the silicon dioxide combined with the underlying silicon wafer. Fig. 7 indicates that the simple model that assumes heat transport through only the silicon dioxide overestimates the heat conductance compared to the experimental results. This overestimation increases with the sensor width and assumes a value of about 30% for  $w = 25 \mu\text{m}$ , and in such cases the thermal resistance of the silicon wafer cannot be ignored.

For the smallest sensor width of  $5 \mu\text{m}$ , the one-layer analytical model (Eq. (8)) is valid, but for larger sensor widths, the two-layer model (Eq. (9)) provides a significantly better accuracy and it can be applied for all the investigated sensors with an accuracy better than 10%. The COMSOL results generally lie slightly below Eq. (9). If the sensor width becomes comparable to the oxide thickness, the full COMSOL model will be needed, as heat transportation in the oxide at the edge of the stack becomes increasingly important.

### 5.2. Effect of liquid

All shown measurements were done in a dry lab-on-a-chip system. For applications, a liquid will be present in the fluidic channel and this could potentially change the result. An illustration of the setup with water can be seen in Fig. 2c. Fig. 8 shows the heat networks for the dry system, where heat transportation through the chip top is neglected, and for the wet system with water in the fluid system, where heat can flow through the protective sensor coating via the water and chip top to the surroundings. We assume that the thermal conductivity of the  $t_{\text{coating}} = 1 \mu\text{m}$  thick Ormocomp coating equals that of  $\text{SiO}_2$  and thus we can write  $R_{\text{coating}} = t_{\text{coating}}/(4lw\kappa_{\text{SiO}_2})$ . However, due to heat dissipation also in the lateral direction,  $R_{\text{top}}$  is harder to estimate and it is better to determine it experimentally. Comparing the cases with and without water, it is seen that the difference in thermal conductivity is  $\Delta G_{\text{eff}} = (R_{\text{coating}} + R_{\text{top}})^{-1}$  and hence that the difference  $\delta T$  in temperature between the sensor and the top

surface of its protective coating is

$$\frac{\delta T}{\Delta T} = \frac{R_{\text{coating}}}{R_{\text{coating}} + R_{\text{top}}} = R_{\text{coating}} \Delta G_{\text{eff}}. \quad (10)$$

We have carried out and analysed measurements of  $\Delta T$  vs.  $I_x$  for a sensor both without and with water in the fluidic system. When the channel was filled with water, we observed an increase of the thermal conductance of  $\Delta G_{\text{eff}} = 6 \times 10^{-4} \text{ }^\circ\text{C/W}$ , which is an order of magnitude smaller than the thermal conductance of the smallest sensor with  $w = 5 \mu\text{m}$ . This shows that the assumption of thermal insulation at the top boundary made in the modeling is well justified. Moreover, from Eq. (10), we find that  $\delta T/\Delta T \approx 9\%$ . This implies that the temperature at the surface of the protective coating in our experimental configuration is close to that of the sensor itself and hence that the sensor self-heating may impact the biology and chemistry taking place on the surface of the sensor coating.

### 5.3. Consequences for applications

The presented work can be used to determine safe sensor operation limits with limited self-heating. For example, in Section 4.2, we found  $I_{\Delta T=1 \text{ }^\circ\text{C}} \approx 16 \text{ mA}$  and  $I_{\Delta T=5 \text{ }^\circ\text{C}} \approx 36 \text{ mA}$  for the sensor geometry used in our previous work [6,8]. In both of these previous studies an rms current of 18 mA was used. From Fig. 5 we observe that the sensor self-heating at this bias current is about  $1.2 \text{ }^\circ\text{C}$  and hence that a possible sensor self-heating of this amount should be taken into consideration.

In Fig. 6 it is observed that  $I_{\Delta T=5 \text{ }^\circ\text{C}}$  sensor width. This is expected as a higher value of  $w$  increases the effective area of the heat flux through the silicon dioxide for a  $w \times w$  sensor square. If, for simplicity, only the  $\text{SiO}_2$  layer is considered, Eqs. (4) and (5) can be rearranged to find the maximum current

$$I_{\Delta T} \approx \sqrt{\frac{G_{\text{eff}} \Delta T}{R}} \approx w \sqrt{\frac{\kappa_{\text{SiO}_2} \Delta T}{t_{\text{SiO}_2} R_s}} \quad (11)$$

where  $R_s$  is the sheet resistance of the sensor. Thus, in agreement with expectations and experimental observations in Fig. 6, sensors with a lower sheet resistance (larger permalloy thickness) can support a larger current for the same allowed self-heating.

When the sensors are used for measurements of magnetic beads magnetized by field due to the sensor current, the sensor signal is proportional to  $I_x^2$  (Eq. (2)). Combining Eqs. (11) and (2) gives the self-field signal

$$V_y \approx \gamma w l \frac{\kappa_{\text{SiO}_2} \Delta T S_0}{t_{\text{SiO}_2} R}. \quad (12)$$

For a fixed value of  $t_{\text{FM}}$  and assuming ideal sensor behavior, the value of  $S_0/R$  is constant [10]. The sensor signal is observed to be proportional to  $l$ , which is in agreement with expectations as the length of each sensor arm does not influence the local sensor heating. However, the maximum sensor bias voltage that can be applied is limited by the integrity of the sensor coating, which thus limits  $l$ . The influence of the width  $w$  of a sensor arm is more complicated as a change in  $w$  also affects  $\gamma$  in a non-trivial manner that depends on the thickness of the protective sensor coating and on how the beads are distributed over the sensor (e.g., if they are on the surface or in a volume over the sensor) [9]. However, generally the value of  $\gamma$  is found to decrease for increasing values of  $w$ . The resulting balance between the decrease of  $\gamma$  and the increase of  $w$  in the product  $\gamma w$  in Eq. (12) has to be evaluated on a case-to-case basis. Decreasing the value of  $w$  may also result in significant shape anisotropy of the sensor stripe, which may modify the sensor behavior.

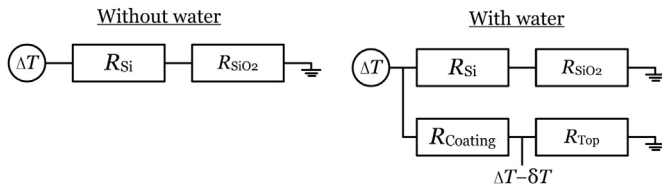


Fig. 8. Heat network considering only heat transport through the underlying silicon wafer (left panel) and including heat transport through the protective sensor coating and the chip top (right panel).  $\Delta T$  is the temperature increase compared the surroundings in the two cases.  $\delta T$  is the temperature drop from the sensor to the top of the sensor protective coating.

Finally, the thickness of the insulating silicon dioxide can be reduced to increase the thermal conductance. This parameter is often disregarded in the design phase. If, for example, the thickness of the silicon dioxide of the present sensors is reduced from the present value of  $t_{\text{SiO}_2} = 1 \mu\text{m}$  to  $0.1 \mu\text{m}$ , the above approximate considerations, that only consider heat conduction through the silicon dioxide, predict that the signal can be increased by up to a factor of 10 for the same allowed sensor self-heating. However, the single-layer approximation is poorly justified in this limit. The more accurate two-layer model predicts more moderate signal increases by factors of 3.5 for  $w = 25 \mu\text{m}$  and 6.2 for  $w = 5 \mu\text{m}$ . For applications of this sensing approach, it may be beneficial to make comparatively short and wide sensors with only a thin insulating oxide underneath. The further study and experimental validation of this will be a topic for future work.

## 6. Conclusion

We have performed a temperature calibration of the bridge resistance for 15 different sensors and used this calibration to determine the sensor self-heating as function of the sensor bias current. We have presented a general model for the effective heat conductance of a resistive sensor system. The maximum sensor bias current that can be applied within a predefined limit of sensor self-heating has been determined both experimentally and theoretically. For our stacks and sensor geometries we have found that the electrically insulating  $1 \mu\text{m}$  thick silicon dioxide layer dominates the thermal resistance. A simple 1D model of heat transfer through  $\text{SiO}_2$  was sufficient to precisely predict sensor heating for sensors with a small area, while a model also including the underlying silicon wafer provided a good description of all measurements. We have found the sensor temperature to be proportional to the Joule heating, and have determined the maximum currents for a  $5^\circ\text{C}$  sensor heating. Such maximum currents are important as the sensor signal scales with the current squared for beads magnetized by the sensor self-field. Consequences for future sensor designs have been discussed.

## Acknowledgments

This work was supported by Copenhagen Graduate School for Nanoscience and Nanotechnology (C:O:N:T), the Knut and Alice Wallenberg (KAW) foundation and the Danish Council for Independent Research (DFR-4005-00116).

## References

- [1] M.A.M. Gijs, F. Lacharme, U. Lehmann, Microfluidic applications of magnetic particles for biological analysis and catalysis, *Chem. Rev.* 110 (3) (2010) 1518–1563.
- [2] G. Reiss, H. Brueckl, A. Huetten, J. Schotter, M. Brzeska, M. Panhorst, D.S. A. Becker, P.B. Kamp, A. Puehler, K. Wojczykowski, P. Jutzi, Magneto-resistive sensors and magnetic nanoparticles for biotechnology, *J. Mater. Res.* 20 (2005) 3294.
- [3] P. Freitas, R. Ferreira, S. Cardoso, F. Cardoso, Magneto-resistive sensors, *J. Phys.: Condens. Matter* 19 (2007) 165221.
- [4] S.X. Wang, G. Li, Advances in giant magneto-resistance biosensors with magnetic nanoparticle tags: review and outlook, *IEEE Trans. Magn.* 44 (2008) 1687.
- [5] R.S. Gaster, D.A. Hall, C.H. Nielsen, S.J. Osterfeld, H. Yu, K.E. Mach, R.J. Wilson, B. Murmann, J.C. Liao, S.S. Gambhir, S.X. Wang, Matrix-insensitive protein assays push the limits of biosensors in medicine, *Nat. Med.* 15 (2009) 1327–1332.
- [6] F.W. Østerberg, G. Rizzi, T. Zardán Gómez de la Torre, M. Strömberg, M. Strømme, P. Svedlindh, M.F. Hansen, Measurements of Brownian relaxation of magnetic nanobeads using planar Hall effect bridge sensors, *Biosens. Bioelectron.* 40 (1) (2013) 147–152.
- [7] F.W. Østerberg, G. Rizzi, M. Donolato, R.S. Bejhed, A. Mezger, M. Strömberg, M. Nilsson, M. Strømme, P. Svedlindh, M.F. Hansen, On-chip detection of rolling circle amplified DNA molecules from *Bacillus globigii* spores and *Vibrio cholerae*, *Small* 10 (14) (2014) 2877–2882.
- [8] G. Rizzi, F.W. Østerberg, M. Dufva, M.F. Hansen, Magneto-resistive sensor for real-time single nucleotide polymorphism genotyping, *Biosens. Bioelectron.* 52 (2014) 445–451.
- [9] T.B.G. Hansen, C.D. Damsgaard, B.T. Dalslet, M.F. Hansen, Theoretical study of in-plane response of magnetic field sensor to magnetic beads magnetized by the sensor self-field, *J. Appl. Phys.* 107 (12) (2010) 124511.
- [10] A.D. Henriksen, B.T. Dalslet, D.H. Skjeller, K.H. Lee, F. Okkels, M.F. Hansen, Planar Hall effect bridge magnetic field sensors, *Appl. Phys. Lett.* 97 (1) (2010) 013507.
- [11] F.W. Østerberg, B.T. Dalslet, D. Snakenborg, C. Johansson, M.F. Hansen, Chip-based measurements of Brownian relaxation of magnetic beads using a planar hall effect magnetic field sensor, *AIP Conf. Proc.* 1311 (2010) 176.